



Published in final edited form as:

J Electron Imaging. 2007 August 6; 16(3): 330091–3300911. doi:10.1117/1.2768092.

Real-time restoration of white-light confocal microscope optical sections

Madhusudhanan Balasubramanian,

Louisiana State University, Department of Computer Science, Baton Rouge, Louisiana 70803, E-mail: madhu@glaucoma.ucsd.edu

S. Sitharama Iyengar,

Louisiana State University, Department of Computer Science, Baton Rouge, Louisiana 70803

Roger W. Beuerman,

National University of Singapore, Yong Loo Lin School of Medicine, Department of Ophthalmology, Singapore Eye research Institute, Singapore 119260, and Nanyang Technical University, Division of Chemical and Biomedical Engineering, Singapore 639798

Juan Reynaud, and

Devers Eye Institute/DIS, 1225 NE Second Avenue, Portland, Oregon 97232

Peter Wolenski

Louisiana State University, Department of Mathematics, Baton Rouge, Louisiana 70803

Abstract

Confocal microscopes (CM) are routinely used for building 3-D images of microscopic structures. Nonideal imaging conditions in a white-light CM introduce additive noise and blur. The optical section images need to be restored prior to quantitative analysis. We present an adaptive noise filtering technique using Karhunen–Loève expansion (KLE) by the method of snapshots and a ringing metric to quantify the ringing artifacts introduced in the images restored at various iterations of iterative Lucy–Richardson deconvolution algorithm. The KLE provides a set of basis functions that comprise the optimal linear basis for an ensemble of empirical observations. We show that most of the noise in the scene can be removed by reconstructing the images using the KLE basis vector with the largest eigenvalue. The prefiltering scheme presented is faster and does not require prior knowledge about image noise. Optical sections processed using the KLE prefilter can be restored using a simple inverse restoration algorithm; thus, the methodology is suitable for real-time image restoration applications. The KLE image prefilter outperforms the temporal-average prefilter in restoring CM optical sections. The ringing metric developed uses simple binary morphological operations to quantify the ringing artifacts and confirms with the visual observation of ringing artifacts in the restored images.

1 Introduction

A confocal microscope allows imaging thick microscopic structures at various depths without physically sectioning the specimen. The concept of confocal microscopy was invented by Marvin Minsky in 1955.¹ A white-light confocal microscope (WLCM) allows imaging tissues *in vivo*.² Use of a white-light source in WLCM reduces speckle noise in the observed images mainly due to the interaction of various wavelengths present in the white light. Figure 1 shows

a schematic representation of a WLCM. An objective lens focuses a thin ray of light passing through a pinhole from a white-light source and illuminates a small volume in the specimen. Assuming that the objective lens has a focal length f and an imaging plane is at a distance i from the objective, then from the lens equation $(1/o)+(1/i)=1/f$, a layer referred to as an *on-focus* layer at a depth o will be on focus. However, the light from the layers neighboring to the on-focus layer, referred to as *out-of-focus* layers, will also be collected by the objective lens. A finitely small pinhole placed at the focal length f limits the photic contributions from the out-of-focus layers and from the locations adjacent to the imaging points in the focal plane, as shown in Fig. 1. When imaging an on-focus layer in the specimen, the whole area needs to be imaged point-by-point. A Nipkow disk with spiral pinhole arrangement is typically used for real-time image formation.

Due to nonideal lens and pinhole size, each image point (pixel) will receive photic contributions from adjacent pixel positions and from out-of-focus planes. The characteristics of the WLCM, which especially accounts for the light from adjacent and out-of-focus planes, can be described using an impulse response of the imaging device commonly known as a point-spread function (PSF) or a smearing function. Assuming that the PSF h of the WLCM is spatially invariant, an image acquired at the image plane can be represented as $g=h*f+n$, where g is the image observed at the image plane, f is the true object image at the object plane, $*$ is the convolution operator, h is the 2-D PSF of the WLCM, and n is the additive noise artifacts introduced by the imaging system.

Image restoration algorithms estimate the original image f from the observed image g with the knowledge of the PSF h^{3-7} or without the knowledge of the PSF h^8 of the imaging instrument. Since image restoration is the reverse of the blurring or convolution process, the image restoration algorithms are commonly referred to as image deconvolution or image deblurring algorithms. For a detailed review of restoration methods, refer to Refs. ⁴ and ⁹.

The performance of the image restoration algorithms, more specifically that of the inverse restoration algorithm, can be improved by prefiltering the image noise.¹⁰ If multiple WLCM images of a specimen at the same z -axis depth are acquired at the same instant, then the images typically will represent the same scene. The only variations among the images in the ensemble, per z -axis depth at a given instant, will be due to the random noise artifacts introduced by the system. In this work, we present a novel adaptive noise filtering algorithm using Karhunen–Loève (KL) expansion for use in confocal microscopes. We use the KL transform to decorrelate an ensemble of WLCM images acquired per z -axis position to filter the random variations in the pixel intensities due to the scanning system and additive noise. Deconvolution is a deblurring process, and the restored images typically exhibit sharp edges with an overall increase in the high-frequency contents of the image. Therefore, we use a gradient-based contrast metric to measure the quality of the restored images. We will compare the performance of the proposed adaptive KL filter with that of a temporal averaging filter in the prefiltering stage during inverse restoration.

Iterative restoration algorithms derive an estimate of f from g in iterative steps.^{6,11} We observed that the images restored using the iterative Lucy–Richardson (LR) deconvolution algorithm exhibit prominent oscillations at a higher number of iterations around the edges and at pixel locations with sharp intensity transitions. These spurious oscillations around the edges are known as *ringing* artifacts. A usual stopping criterion for an iterative restoration algorithm is an error functional of the form $\min \|g-h*\hat{f}_k\|$, where \hat{f}_k is an estimate of the original image f at the k th iteration. The ringing artifacts usually do not appear in the forward projection $h*\hat{f}_k$. Therefore, terminating the iterations prior to convergence imposes a prior model on the restored image \hat{f}_k . Truncation of iterations in an iterative restoration algorithm is a well-known regularization technique (called regularization via truncated iterations).^{6,9} These ringing

artifacts can be easily identified by a human visual system (HVS). Hence, an image-quality-based *ringing metric* will be useful to identify an appropriate stopping criterion for the iterative LR deconvolution algorithm.

Recently, several image-quality metrics have been proposed to measure the blur and blocking artifacts introduced by image/video compression algorithms.^{12–14} Objective quality metrics such as the peak signal-to-noise ratio (PSNR) and mean-squared error (MSE) metrics do not correlate with the quality assessed by an HVS.^{15,16} A frequency-based ringing metric will have difficulties in differentiating the ringing artifacts from the image features. Spatial analysis techniques, as in Ref. 13, require extensive row-by-row processing and are not suitable for real-time image-quality measurement. We have developed a novel ringing metric using simple binary morphological operations to measure the amount of ringing artifacts present in an image.

Section 2 contains a brief overview of KL expansion. In Sec. 3, we present the adaptive noise filtering and inverse restoration algorithm using KL expansion. In Sec. 4, we describe a sobel operator-based contrast measure for evaluating the performance of the WLCM image restoration. We present our ringing metric for use with the iterative LR deconvolution algorithm in Sec. 5. In Sec. 6, we present and discuss the results of (1) WLCM image restoration using adaptive KL noise prefiltering and inverse restoration algorithm and compare the results with temporal-average prefiltering algorithm and (2) the performance of the ringing metric in estimating the ringing artifacts introduced in the WLCM images restored using LR deconvolution algorithm. We conclude this work in Sec. 7.

2 Karhunen–Loève Expansion

Karhunen–Loève (KL) expansion provides an optimal set of orthogonal basis vectors that span an entire ensemble of signal,¹⁷ The KL transform is optimal, in a mean-squared-error sense, over all the images drawn from distributions with the same covariance matrix R . It is also referred to as proper orthogonal decomposition (POD), hoteling transform, and principal component analysis (PCA).¹⁸ KL expansion decorrelates a given ensemble of signals by discovering an orthogonal basis set that is optimal for the signal under consideration as opposed to analyzing the signal using an off-the-shelf wavelet basis or Fourier transform. It has been used for characterizing an ensemble of human faces with few optimal image bases called eigenpictures, thereby reducing the number of coefficients in the KL expansion for each image.¹⁹

Using KL expansion, a continuous second-order process $x \in \mathbb{R}^{M \times N}$ with a covariance $R(x, x')$ can be expanded as

$$x = \sum \alpha_n \phi_n(x), \quad (1)$$

with $E(\alpha_i, \alpha_j) = \sqrt{\lambda_i} \delta_{ij}$ and $\langle \phi_i, \phi_j \rangle = \delta_{ij}$. Here E is the expectation, $\{\lambda_i\}$ are the eigenvalues, and $\{\phi_i\}$ are the eigenvectors of the covariance matrix R of $\{x_i\}$. In the discrete case,

$$R\Phi = \Lambda\Phi. \quad (2)$$

The existence of $\Lambda = \{\lambda_i\}$ and $\Phi = \{\phi_i\}$ in Eq. (2) is guaranteed by Mercer's theorem²⁰ analogous to the spectral decomposition of symmetric matrices.²¹ For a given ensemble $\{x_i\}_{i=1}^L$, KL expansion guarantees the best k -term orthogonal expansion (in a mean-squared-error sense) among all the orthogonal transforms.²² The eigenvectors of the covariance matrix R form an optimal orthogonal basis for the ensemble $\{x_i\}_{i=1}^L$. The orthogonal basis vector ϕ_i corresponding

to the largest eigenvalue is in the principal direction of the ensemble $\{x_i\}_{i=1}^L$. When the elements in the ensemble $\{x_i\}_{i=1}^L$ are correlated, for example, for an ensemble is formed using multiple snapshots of images of a given scene, each with different noise realization, the principal basis vector alone can effectively represent the entire ensemble with the least expansion error when compared to the other available orthogonal expansions. This property is desirable in pattern recognition applications. The energy retained during a k -term expansion is given in terms of the eigenvalues of R as follows:

$$\frac{\sum_{i=1}^k \lambda_i}{\sum_{i=1}^{MN} \lambda_i} \times 100\% . \quad (3)$$

The eigenvectors and eigenvalues of R can be computed using a direct computation or using a reduced computation technique called the method of snapshots.²³

Let $\{x_i\}_{i=1}^L$ be the expectation-centered ensemble set, where $x_i \in \mathbb{R}^{M \times N}$ and $E(x)=0$. Let each of the column formatted ensemble elements x_i form the i th column of the ensemble matrix X . For example, given an ensemble $\{x_i\}_{i=1}^L$ of gray-scale images of size 256×256 , each of the column-formatted images $x_i \in \mathbb{R}^{65536 \times 1}$ will form the i th column of the ensemble matrix $X \in \mathbb{R}^{65536 \times L}$. Here, \mathbb{R} represents the space of gray-scale image vectors, and L is the number of elements in the ensemble. Now, the ensemble covariance matrix $R=XX^T$, where $R \in \mathbb{R}^{MN \times MN}$.

2.1 Direct Method to Compute the Optimal Basis

The eigenvectors $\{\phi_i\}_{i=1}^{MN}$ of the ensemble covariance R in Eq. (2) that form the orthogonal basis for the ensemble can be derived using a singular-value decomposition (SVD) of the ensemble matrix X as follows:

$$X=U\Lambda V, \quad (4)$$

$$\text{covariance } R=XX^T=U\Lambda VV^T \Lambda U^T=U\Lambda^2 U^T. \quad (5)$$

The covariance XX^T is a symmetric matrix; therefore, an eigendecomposition as in Eq. (5) exists. The left singular matrix U forms the basis of the column space of the ensemble matrix X as in Eq. (4); and therefore, the ensemble elements $\{x_i\}_{i=1}^L$, which form the column space of X , have an expansion in U . Solving the eigenvalue problem in Eq. (5) requires solving an $MN \times MN$ system. In the above example of a gray-scale image ensemble, this would require solving a $65,536 \times 65,536$ system. Although computational resources are available for solving such a massive eigenvalue problem, it is unnecessary for the problem under consideration.

2.2 Method of Snapshots

The dimension of the optimal orthogonal basis needed to describe the ensemble is L , where L is the ensemble size. The ensemble matrix X is singular and does not require a full dimension to describe the ensemble elements. Thus, a reduction in the basis computation can be achieved using a reduced SVD approach as follows:

$$X^T X=V^T \Lambda U^T U \Lambda V=V^T \Lambda^2 V. \quad (6)$$

The right singular vectors V and the eigenvalues Λ^2 can be computed from Eq. (6). This requires solving an $L \times L$ system. Further, the left singular vectors U can be computed from Eq. (4) using X , V , and Λ . The left singular vectors U span the column space of the ensemble matrix X and thus form the basis of the ensemble $\{x_i\}_{i=1}^L$. The reduced SVD approach for determining an optimal ensemble basis¹⁷ provides a significant reduction in computation when $L \ll MN$.

3 Adaptive Noise Filtering and Restoration of WLCM Images

The WLCM optical section images are digitized using a frame grabber (DT 3155) PCI card that allows a maximum frame acquisition rate of 30 frames per second. The frame acquisition rate will be limited by the scanning rate of the confocal microscope. To adaptively filter noises in the acquired images, we propose using 3 frames of images acquired per z -axis position. Each of the images is converted to a column-formatted image $X_i \in \mathbb{R}^{MN \times 1}$. An ensemble matrix $X \in \mathbb{R}^{MN \times 3}$ is constructed using the column-formatted images. The vector space $\mathbb{R}^{MN \times 1}$ represents the space of gray-scale WLCM images. From the KL expansion using the method of snapshots, the dimension of the ensemble space can be reduced to three. An optimal basis for this ensemble matrix X can be obtained by computing the eigenvectors V of the covariance matrix $X^T X \in \mathbb{R}^{3 \times 3}$ and the left singular matrix $U \in \mathbb{R}^{MN \times 3}$ of X as described in Sec. 2.2. Now each of the column-formatted ensemble images X_i can be expressed as a linear combination of the optimal

$$\text{basis as } X_i = \sum_{j=1}^3 \langle X_i, U_j \rangle U_j.$$

Since the ensemble matrix is formed using the images of the same scene, we found that only the first principal left singular vector of X , denoted U_{\max} , is sufficient to retain more than 90% of the energy. Note that the bases $\{U_1, U_2, U_3\}$ are arranged in the order of their contribution in the ensemble space with $U_1 = U_{\max}$. The first principal component U_1 points in the direction of the maximal ensemble variance and therefore typically represents the features present in the image ensemble. The second and third principal components are available to depict the differences between the three images in the ensemble and contain less than 10% of the total ensemble energy. Since the ensemble was formed using the images of the specimen at the same z -axis depth, the coefficients of the second and third principal components can be dropped to eliminate the variations observed between the images in the ensemble. These coefficients typically represent the noise and random pixel variations due to the scan lines introduced by the Nipkow scanning disk. Thus, any image from the ensemble reconstructed using only the first principal component will be a noise-filtered image of the specimen at the given z -axis depth given by

$$X_{\text{filtered}} = \langle X_i, U_1 \rangle U_1, \quad (7)$$

where X_i can be any one of images from the ensemble. Now the filtered image can be restored using the inverse restoration algorithm. Algorithm 1 summarizes the adaptive noise filtering and the restoration steps.

Algorithm 1 Algorithm for adaptive KL prefiltering and inverse restoration

-
- 1 **procedure** KL PREFILTER-INVERSE RESTORATION
 - 2 Acquire image ensemble $\{x_j\}_{j=1}^3$ at a given z -axis position.
 - 3 Form column-formatted image matrices $\{x_j\}_{j=1}^3$ and ensemble matrix X .
 - 4 Compute the covariance matrix $R = XX^T$.

- 5 Compute an optimal ensemble basis $\{u_p\}_{p=1}^3$ using reduced SVD as in Sec. 2.2.
- 6 Filter the noise and random components in the image ensemble by dropping the second and third principal components. Determine the noise filtered image as in Eq. (7).
- 7 Using the optical transfer function H and the noise prefiltered image X_{filtered} , restore image as $\overline{X_{\text{restored}}} = H^{-1} \overline{X_{\text{filtered}}}$, where X represents the FFT of X .
- 8 Energy retained during the adaptive KL prefiltering $\lambda_{\text{max}} / \sum_{i=1}^3 \lambda_i \times 100 \%$.
- 9 **end procedure**

4 Evaluation of the Restored Images Using a Contrast Measure

If the PSF of the WLCM were ideal, $h(x, y) = \delta(x, y)$. However, nonideal lens and pinhole dimension result in a PSF that acts as a low-pass filter, resulting in a blurred image. The image restoration process restores an image using a prior knowledge about the PSF of the imaging device. The blur in the restored images is expected to decrease and cause an eventual increase in the high-frequency details in the image. The common choices to measure blur in images are (1) image pixel intensity variance; (2) l_1 -norm of the image gradient ∇I , (3) l_2 -norm of the image gradient ∇I , (4) l_1 -norm of the image Laplacian $\nabla^2 I$, and (5) l_2 -norm of the image Laplacian $\nabla^2 I$. Autofocusing in widefield microscopy requires a similar focus measure to identify an optimal focusing point with less blur.^{24–27}

We use an image contrast measure of the l_2 -norm of the image gradient to demonstrate the performance of the adaptive KL filter presented in Sec. 3. The image gradient is given as

$$\nabla I = \begin{pmatrix} G_x \\ G_y \end{pmatrix} = \begin{pmatrix} \partial I / \partial x \\ \partial I / \partial y \end{pmatrix}.$$

Here, the image x - and y -gradients (G_x, G_y) are computed using the sobel operator kernels

$$S_x = \begin{pmatrix} -1 & 0 & 1 \\ -2 & 0 & 2 \\ -1 & 0 & 1 \end{pmatrix} \quad \text{and} \quad S_y = \begin{pmatrix} -1 & -2 & -1 \\ 0 & 0 & 0 \\ 1 & 2 & 1 \end{pmatrix}$$

as $G_x = S_x * I$ and $G_y = S_y * I$, respectively. Now the magnitude of the image gradient at all the pixel locations can be computed as

$$\nabla I = \text{magnitude}(\nabla I) = \sqrt{G_x^2 + G_y^2}. \quad (8)$$

Using the image gradient in Eq. (8), we can compute the contrast of an image $I \in \mathbb{R}^{M \times N}$ as follows:

$$\text{contrast measure} = \sum_{i=1}^M \sum_{j=1}^N (\nabla I(i, j) - \overline{\nabla I})^2, \quad (9)$$

where $\overline{\nabla I}$ is the mean image gradient computed as $\overline{\nabla I} = (1/MN) \sum_{i=1}^M \sum_{j=1}^N \nabla I(i, j)$.

5 A Ringing Metric for Use with the Iterative Lucy–Richardson Deconvolution Algorithm

We attempted to quantify the amount of deblurring achieved in each iterative step using the contrast measure defined in Eq. (9) using the iterative Lucy–Richardson (LR) deconvolution³ defined as

$$\widehat{f}_{k+1}(x, y) = \widehat{f}_k(x, y) \left(\frac{h(-x, -y) * g(x, y)}{h(x, y) * \widehat{f}_k(x, y)} \right). \quad (10)$$

We observed that the contrast measure indicated an increasing trend during iterative LR restoration steps. We expected the contrast measure to converge to a maximum contrast value. But the contrast measure was exponentially increasing at each iterative step. Upon careful evaluation of the restored images at various iterative steps, we observed significant oscillations around edges and at pixel locations with sharp intensity transition in the restored images at higher number of iterations. Figure 2 shows the contrast plot of an image of random cotton fibers at various iterative steps of the LR deconvolution algorithm.

The PSF h in the imaging model $g = h * f$ integrates pixel intensities from adjacent locations to cause blurring in the acquired image g . The restoration process computes pixel gradients using an inverse of the optical transfer function (Fourier transform of the PSF matrix). Therefore, the locations in the image with sharp intensity transition exhibit pixel intensity overshoot (extreme positive values) or undershoot (extreme negative values).⁴ The ringing artifacts appear as oscillations around the edges or locations with sharp intensity transitions. This led us to develop a ringing metric to quantify the amount of ringing introduced at various iterative steps to assist in identifying an appropriate terminal point of the iterative LR deconvolution algorithm.

The proposed ringing metric uses the edge profiles of the observed image g and the edge profiles of the images restored \widehat{f}_k to isolate the ringing artifacts introduced during restoration. The area surrounding the edge profiles of the original image are the regions to be observed for ringing artifacts. The edge profile $E_{\text{ref}}(g)$ of the original image g can be extracted using the canny edge detector.³ From the edge profile $E_{\text{ref}}(g)$, the ringing region around the edges can be defined by dilating $E_{\text{ref}}(g)$ with an $r \times r$ structuring element (SE), where r is the approximate width in number of pixels from an edge to cover the ringing artifacts. The dilation operation is defined as follows:

$$E_{\text{RingRegion}}(g) = E_{\text{ref}}(g) \oplus SE = (E_{\text{ref}}^c(g) \ominus \widetilde{SE})^c, \quad (11)$$

where \oplus is a binary dilation operator and \ominus is a binary erosion operator defined as $E_{\text{ref}}(g) \ominus SE = \{x: SE_x \subset E_{\text{ref}}\}$. $E_{\text{ref}}^c(g)$ is the binary complement of $E_{\text{ref}}(g)$, SE is the structuring element, \widetilde{SE} is the rotation of the structural element by 180° , and SE_x is the translation of SE by x .²⁸ At the end of each iterative step k , an edge profile $E(\widehat{f}_k)$ of the restored image \widehat{f}_k can be determined. Now the edges and any ringing artifacts around the original edges $E_{\text{ref}}(g)$ can be selected from $E(\widehat{f}_k)$ by a simple pixelwise logical AND operation between $E_{\text{RingRegion}}(g)$ and $E(\widehat{f}_k)$. Since restoration preserves the edges present in the original image g , the additional edges observed around the reference edge profile in the restored image typically represent the ringing artifacts. The ringing metric is defined

$$\text{ringing metric} = \frac{\sum_{i=1}^M \sum_{j=1}^N [E_{\text{RingRegion}}(g) \text{ AND } E(\hat{f}_k)] - \sum_{i=1}^M \sum_{j=1}^N E_{\text{ref}}(g)}{\sum_{i=1}^M \sum_{j=1}^N E_{\text{ref}}(g)}. \quad (12)$$

6 Results

The PSF of the WLCM was experimentally determined by imaging 5-micron-diameter microspheres under the usual imaging conditions. Several frames of microsphere images at the same focus were averaged to reduce the noise sensitivity of the PSF. A single microsphere was isolated and cropped from the image and was used to determine the PSF of the WLCM. The background of the cropped microsphere image was kept to a minimum to avoid oscillations in locations of sharp intensity transitions in the restored images. Figure 3(a) shows the image of a microsphere and Fig. 3(b) shows the surface plot of the PSF of the WLCM.

Figures 4(a)–4(c) show the image ensemble of a random cotton fiber at the same z -axis depth. The KL basis computed using the reduced SVD method is shown in Figs. 4(d)–4(f). It is clear from the optimal ensemble basis that the first principal vector retains most of the energy in the ensemble (95.5%). Figure 4(g) shows the inverse restored image after temporal-average prefiltering, and Fig. 4(h) shows the inverse restored image after adaptive KL prefiltering. Restoration results on similar cotton fibers and images of lamina cribrosa of cow retina at 12 mmHg of intraocular pressure (IOP) level are shown in Fig. 5 and Fig 6. All the optical sections included in this study and presented here are actual WLCM observations (and not simulations using an artificial PSF and noise). A contrast measure plot in Fig. 7 shows the contrast measures of the restored images after temporal-average and adaptive KL prefiltering. The adaptive KL prefiltering outperforms the temporal-average prefiltering in all experimental cases. Also, a visual evaluation of the image restored after adaptive KL prefiltering shows improvement over the temporal-average prefiltered images. Ensembles of a random cotton fiber with ensemble sizes of 5, 7, and 9 were used to study the performance of the temporal-average and adaptive KL prefilter on increasing the ensemble size. Figure 8 shows an optical section image from the ensemble, images restored, and contrast measure performance on increasing the ensemble size for prefiltering. The contrast measures of the images restored using adaptive KL prefilter increases upon increasing the ensemble size.

Figure 9(b) shows an image of random cotton fibers superimposed with its edge profile. Figure 9(d) shows the edge profile $E(\hat{f}_6)$ of a restored image at iteration 6 of the LR deconvolution algorithm superimposed with the reference edge profile $E_{\text{ref}}(g)$ and a binary edge mask $E_{\text{RingRegion}}(g)$ for selecting the region around $E_{\text{ref}}(g)$. Ringing artifacts can be observed around the edges in the restored image \hat{f}_6 in Fig. 9(c). Visual inspection of the images restored at higher iterative steps of the LR deconvolution algorithm confirms the increasing trend of the ringing metric plot shown in Fig. 9(e).

7 Conclusion

We have presented an adaptive noise filtering technique by discovering an optimal basis from an ensemble of 3 images acquired per z -axis position. The noise and random components are filtered by dropping the second and third principal components of the basis. A reduced SVD or snapshot method of determining the basis makes this technique suitable for real-time restoration of WLCM images. The noise-filtering algorithm proposed here does not require prior knowledge of the type of noise present in the system and hence adaptive to the images being restored. The adaptive KL prefilter significantly reduces the random image artifacts and noise in the WLCM images. The proposed adaptive noise-filtering algorithm can be used in

the prefiltering stage of image deconvolution algorithms to improve the convergence of iterative restoration algorithms and to improve the quality of the images restored using a simple inverse restoration method. Also, the adaptive KL prefilter shows promises for further improvement in the restored images on increasing the ensemble size of the raw optical sections acquired per z -axis position. As indicated by the ringing metric, visual inspection of the images restored at various iterative steps of the LR deconvolution algorithm confirms the increase in the ringing artifacts during restoration. The proposed ringing metric is less sensitive to noise amplification during restoration and is computationally efficient, making it suitable for real-time image-quality evaluation. While the ringing metric was developed and demonstrated for use with the iterative LR deconvolution algorithm, it should be applicable to other iterative restoration algorithms that introduce prominent ringing artifacts in the restored images.

Acknowledgments

This publication was made possible by NIH Grant Number P20 RR16456 from the INBRE Program of the National Center for Research Resources. Its contents are solely the responsibility of the authors and do not necessarily represent the official views of the NIH.

References

1. Minsky, M. Microscopy apparatus. U.S. Patent. 3013467. 1961 Dec.
2. Kaufman, SC. PhD thesis. Louisiana State University School of Medicine; 1996. The development and application of a white-light confocal microscope in the morphologic and anatomic characterization of cells within the cornea.
3. Gonzalez, RC.; Woods, RE. Digital Image Processing. 2nd ed.. Englewood Cliffs, NJ: Prentice-Hall; 2002.
4. Andrews, HC.; Hunt, BR. Digital Image Restoration. Englewood Cliffs, NJ: Signal Processing Series, Prentice-Hall; 1977.
5. Banham MR, Katsaggelos AK. Digital image restoration. IEEE Signal Process. Mag 1997;24–41.
6. Biemond J, Lagendijk RL, Mersereau RM. Iterative methods for image deblurring. Proc. IEEE 1999;19:373–385.
7. Jansson, PA. Deconvolution of Images and Spectra. 2nd ed.. Boston: Academic Press; 1997.
8. Kundur D, Hatzinakos D. Blind image deconvolution. IEEE Signal Process. Mag 1996;43–63.
9. Lagendijk, RL.; Biemond, J. Iterative Identification and Restoration of Images. Boston: Kluwer Academic Publications; 1991.
10. Van Kempen GMP, Van Vliet LJ. Dutch Society for Pattern Recognition and Image Processing, Drift. Prefiltering: Reducing the noise sensitivity of non-linear image restoration algorithms. Fourth Quinquennial Review 1996–2001 2001:411–422.
11. Nagy JG, Lee KP, Perrone L. Iterative methods for image restoration: A matlab object oriented approach. Numer. Algorithms 2004;36:73–93.
12. Wang Z, Bovik AC. A universal image quality index. IEEE Signal Process. Lett 2002;9(3):81–84.
13. Marziliano P, Dufaux F, Winkler S, Ebrahimi T. Perceptual blur and ringing metrics: Application to JPEG-2000. Elsevier Signal Processing: Image Comm 2004;19(2):163–172.
14. Lai Y-K. A Haar wavelet approach to compressed image quality measurement. J. Visual Commun. Image Represent 2000;11:17–40.
15. Ong E, Lin W, Lu Z, Yang X, Yao S, Pan F, Jiang L, Moschetti F. A no-reference quality metric for measuring image blur. Seventh Int. Symp. Signal Processing and Its Appl 2003:469–472.
16. Wang Z, Bovik AC, Lu L. Why is image quality assessment so difficult? IEEE Int. Conf. Acoustics, Speech and Signal Processing. 2002
17. Kirby, M. Geometric Data Analysis—An Empirical Approach to Dimensionality Reduction and the Study of Patterns. New York: John Wiley & Sons, Inc.; 2001.
18. Jain, AK. Fundamentals of Digital Image Processing. Englewood Cliffs, NJ: Prentice-Hall; 1988.

19. Sirovich L, Kirby M. Low-dimensional procedure for the characterization of human faces. *J. Opt. Soc. Am. A* 1987;4(3):519–524. [PubMed: 3572578]
20. Riesz, F.; Nagy, BS. *Functional Analysis*. Boron, LF., editor. New York: Frederick Ungar Publishing Co.; 1955. translated by
21. Trefethen, LN.; Bau, D, III. *Numerical Linear Algebra*. Philadelphia: SIAM; 1997.
22. Dür A. On the optimality of the discrete Karhunen-Loève expansion. *SIAM J. Control Optim* 1998;36(6):1937–1939.
23. Sirovich L. Turbulence and the dynamics of coherent structures—Part I—Coherent structures. *Q. Appl. Math* 1987;XLV(3):561–571.
24. Pech-Pacheco JL, Cristóbal G, Chamorro-Martínez J, Fernández-Valdivia J. Diatom autofocussing in brightfield microscopy: A comparative study. *Proc. 15th Int. Conf. Patt. Recog* 2000:314–317.
25. Nayar SK, Nakagawa Y. Shape from focus. *IEEE Trans. Pattern Anal. Mach. Intell* 1994;16(8):824–831.
26. Yap PT, Raveendran P. Image focus measure based on chebyshev moments. *IEE Proc. Vision Image Signal Process* 2004;151(2):128–136.
27. Shah, UB.; Nayar, SK. Extracting 3-D structure and focused images using an optical microscope. Section 5A: Three-Dimensional Image Processing; Fifth Annual IEEE Symposium on Computer-Based Medical Systems; 1992. p. 292-301.
28. Dougherty, ER.; Lotufo, RA. *Hands-on Morphological Image Processing*. Bellingham, WA: SPIE; 2003.

Biographies



Madhusudhanan Balasubramanian is currently a postdoctoral research fellow at the Hamilton Glaucoma Center, University of California, San Diego. He received his diploma from Muthiah Polytechnic, India, in 1995 and his BE degree from PSG College of Technology, India, in 1998, both in electrical and electronics engineering. He earned his MS degree in systems science in 2003 and his PhD in computer science in 2006 from Louisiana State University, Baton Rouge. His research interests are in biomedical optical instruments for imaging microscopic structures, developing computer vision and image processing algorithms,

and applied mathematical and statistical approaches for studying structural deformation in biological structures.



S. Sitharama Iyengar is the chairman and Roy Paul Daniels Chaired Professor of Computer Science at Louisiana State University, Baton Rouge and is also the Satish Dhawan Chaired Professor at the Indian Institute of Science, Bangalore. His publications include 6 textbooks and over 380 research papers. His research interests include high-performance algorithms, data structures, sensor fusion, data mining, and intelligent systems. His research has been funded by the NSF, ONR, NASA, DoE/ORNL, U.S. Army Research Office, and the DARPA and MURI Programs. He is a fellow of IEEE, ACM, AAAS, and SDPS. He is a recipient of IEEE awards, best paper awards, the Distinguished Alumnus award of the Indian Institute of Science, Bangalore, and other awards. He has served as the editor of several IEEE journals and is the founding editor-in-chief of the International Journal of Distributed Sensor Networks.



Roger W. Beuerman is currently the deputy/scientific director of the Singapore Eye Research Institute and adjunct professor of ophthalmology at the Department of Ophthalmology at the Yong Loo Lin School of Medicine of the National University of Singapore. He has been working on the development of the white-light confocal microscopy for the ophthalmology clinic since 1994 and with his colleagues developed an FDA-approved machine. Imaging the status of fungal infections in the cornea of the eye and the fingernail showed that imaging the organism was a rapid, noninvasive method of diagnosis of the disease at these two vulnerable sites. However, image noise is an issue in the clinical application and, as there is usually just one opportunity for image collection to utilize a set of operations to eliminate noise, is important for clinical use.

Juan Reynaud is a systems analyst at the Devers Eye Institute in Portland, Oregon. He received his BS and MS degrees in electrical engineering from the University of New Orleans in 1990 and 1992, respectively. His interests include developing image processing algorithms for biomedical data analysis and 3-D data visualization.



Peter Wolenski received his PhD in mathematics from the University of Washington in 1988. His research specialty is optimal control and variational analysis, and he has published 1 book and over 35 research articles. He is currently the “Russell B. Long” Professor of Mathematics at Louisiana State University.

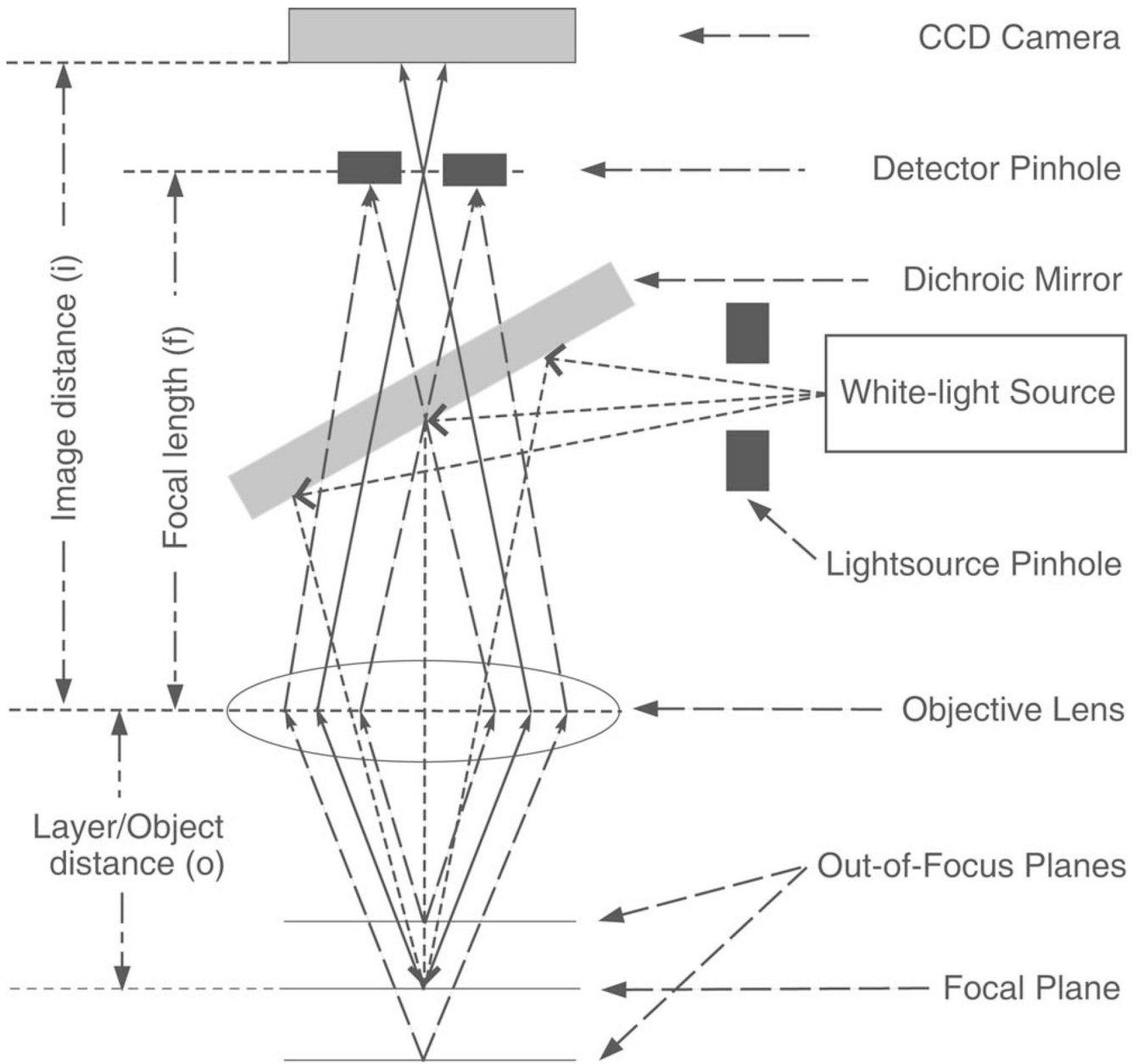
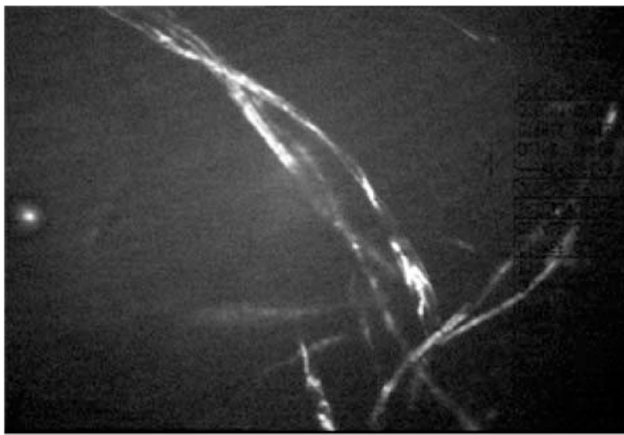
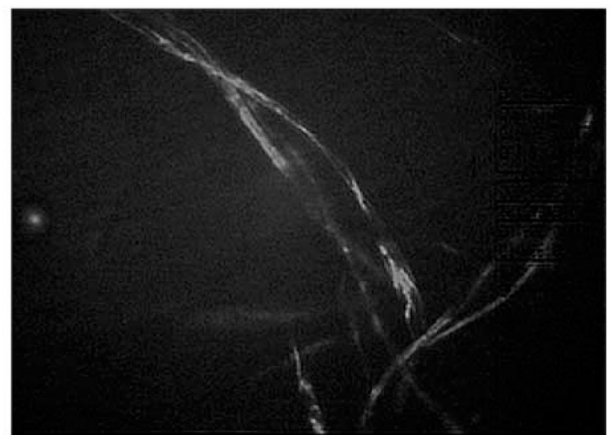


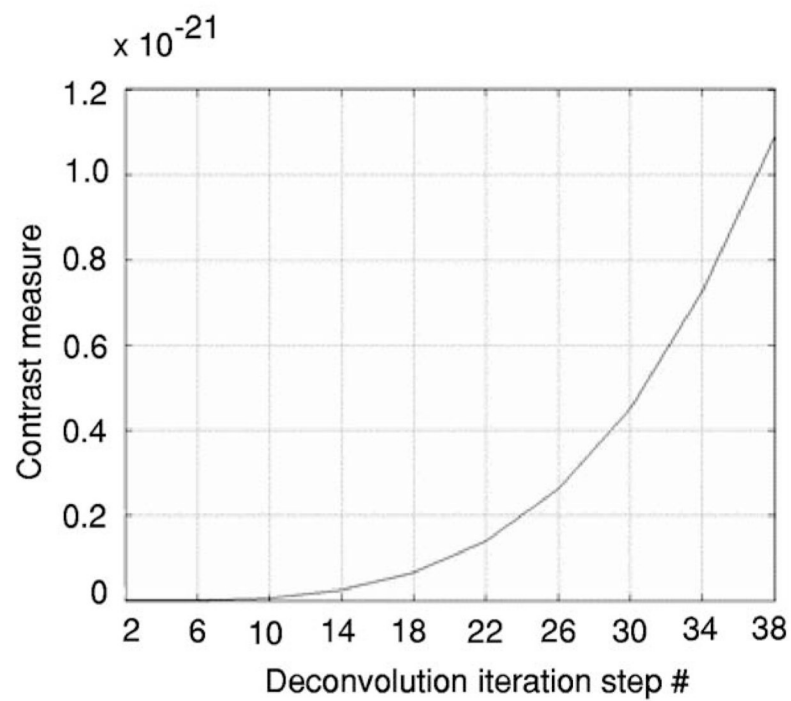
Fig. 1. Schematic representation of a white-light confocal microscope.



(a) Unprocessed optical section image

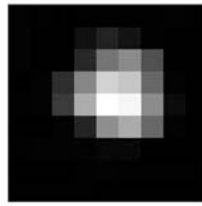


(b) Iteration # 10

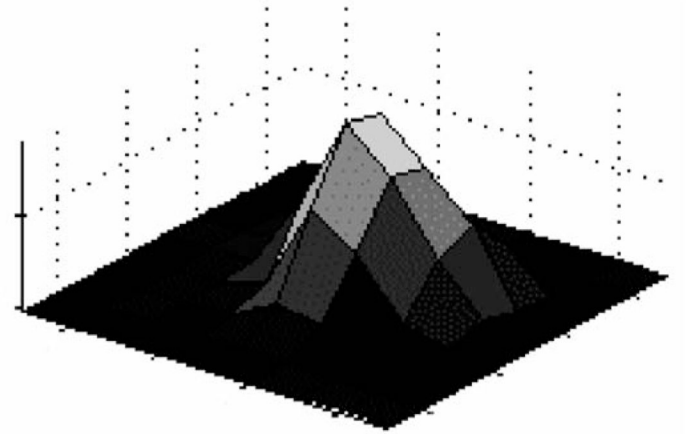


(c) Contrast plot

Fig. 2. Image of random cotton fibers restored using the Lucy-Richardson restoration algorithm; contrast measure increases exponentially due to ringing artifacts.



(a) Image of a 5-micron sphere



(b) Intensity plot of PSF

Fig. 3.
Experimental PSF of the WLCM determined by imaging 5-micron-diameter spheres.

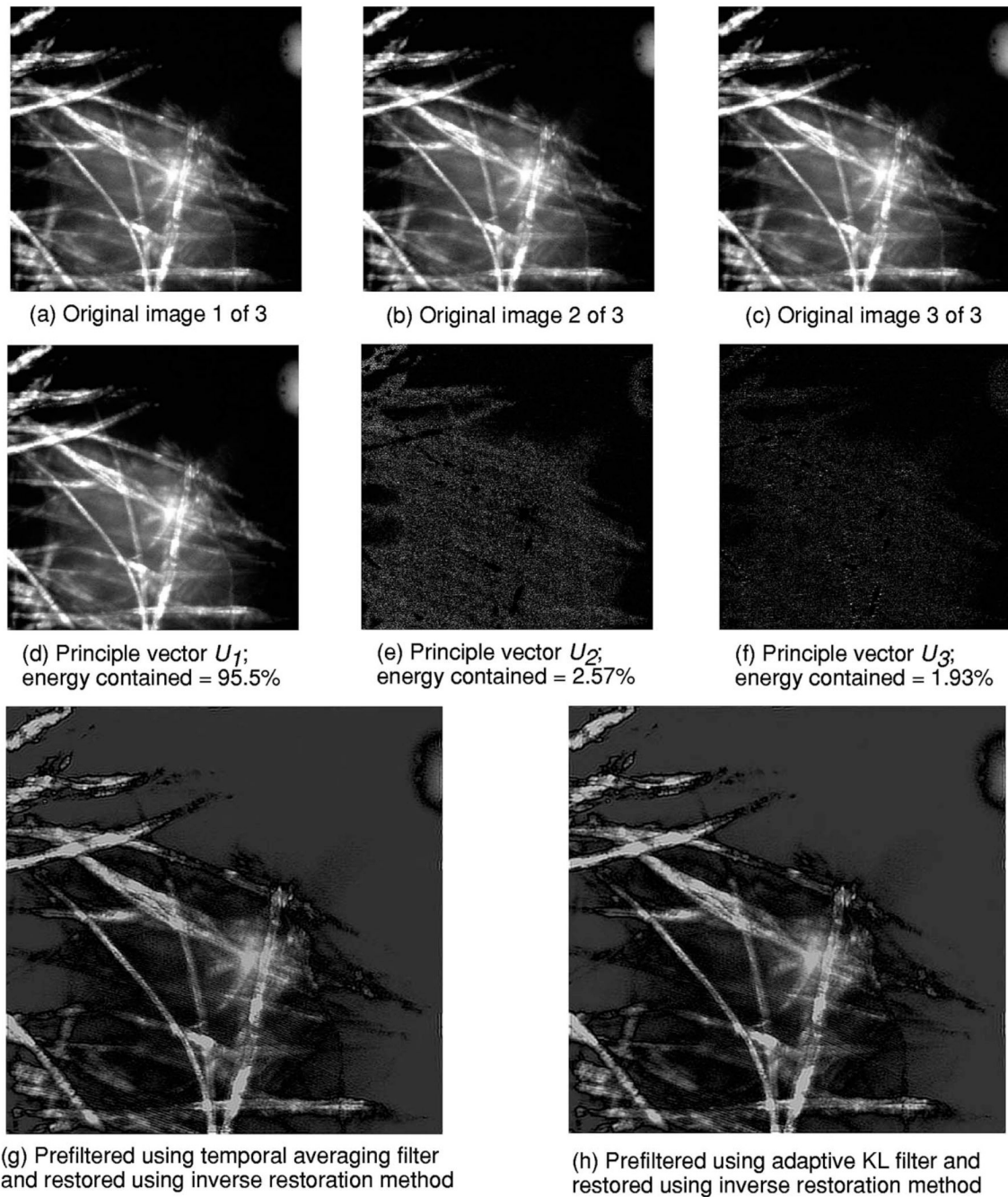
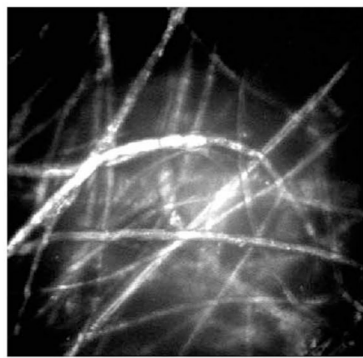
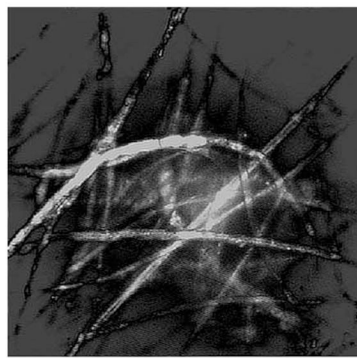


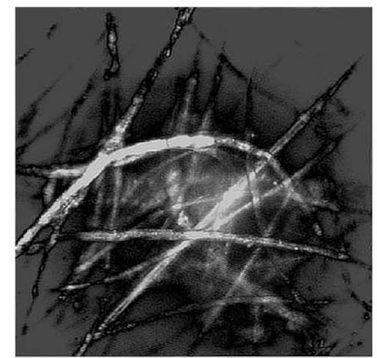
Fig. 4. Ensemble of random cotton fiber images, their KL decomposition, and the inverse restored images after temporal-average and adaptive KL prefiltering.



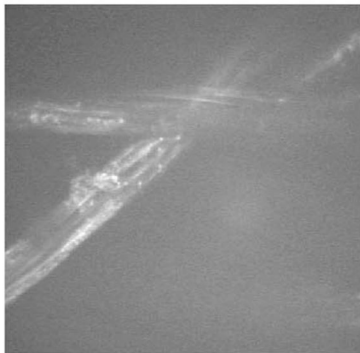
(a) Unprocessed image from an ensemble of 3 optical sections



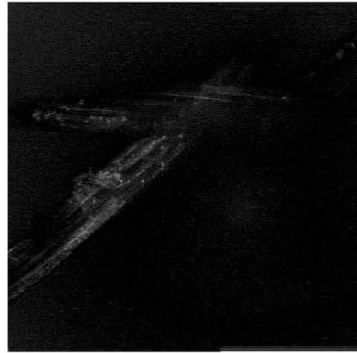
(b) Restored after temporal-average prefiltering



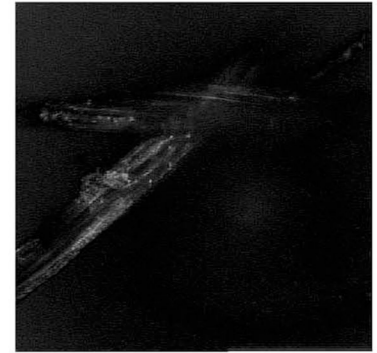
(c) Restored after adaptive KL prefiltering



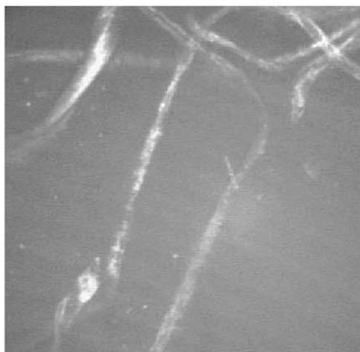
(d) Unprocessed image from an ensemble of 3 optical sections



(e) Restored after temporal-average prefiltering



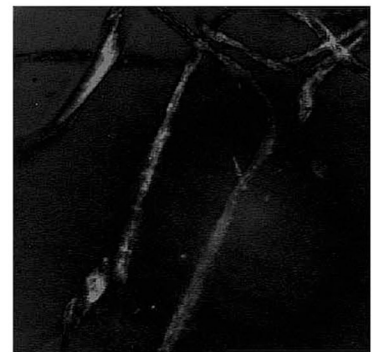
(f) Restored after adaptive KL prefiltering



(g) Unprocessed image from an ensemble of 3 optical sections

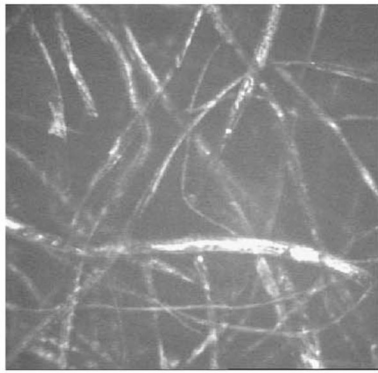


(h) Restored after temporal-average prefiltering

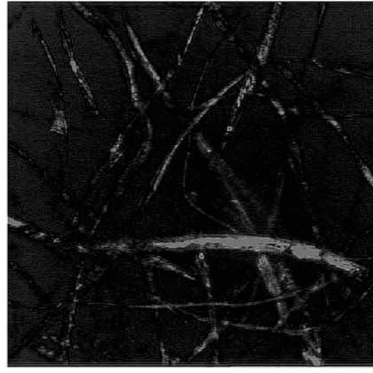


(i) Restored after adaptive KL prefiltering

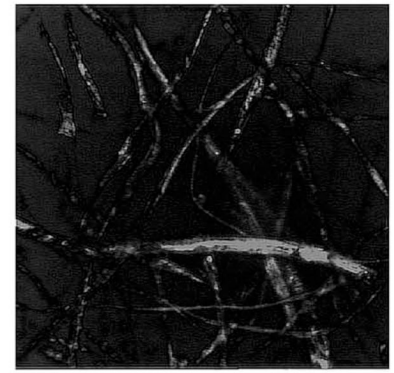
Fig. 5. Random cotton fibers (a, d, g) restored using inverse filter deconvolution after prefiltering random artifacts using temporal averaging filter (b, e, h) and adaptive KL filter (c, f, i).



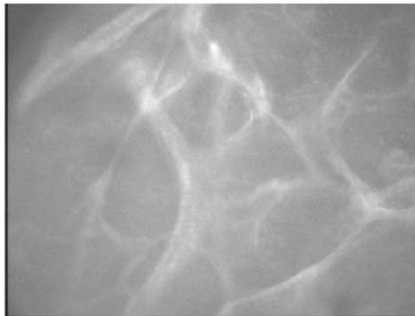
(a) Unprocessed image from an ensemble of 3 optical sections



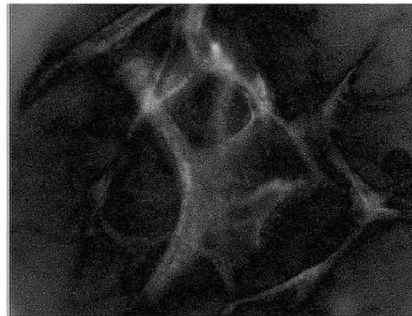
(b) Restored after temporal-average prefiltering



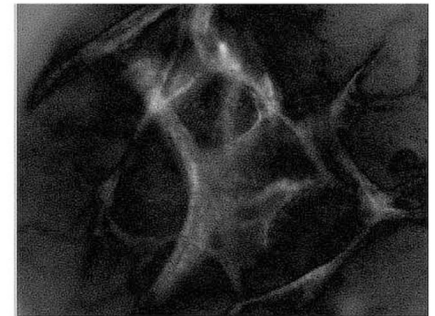
(c) Restored after adaptive KL prefiltering



(d) Unprocessed image from an ensemble of 3 optical sections



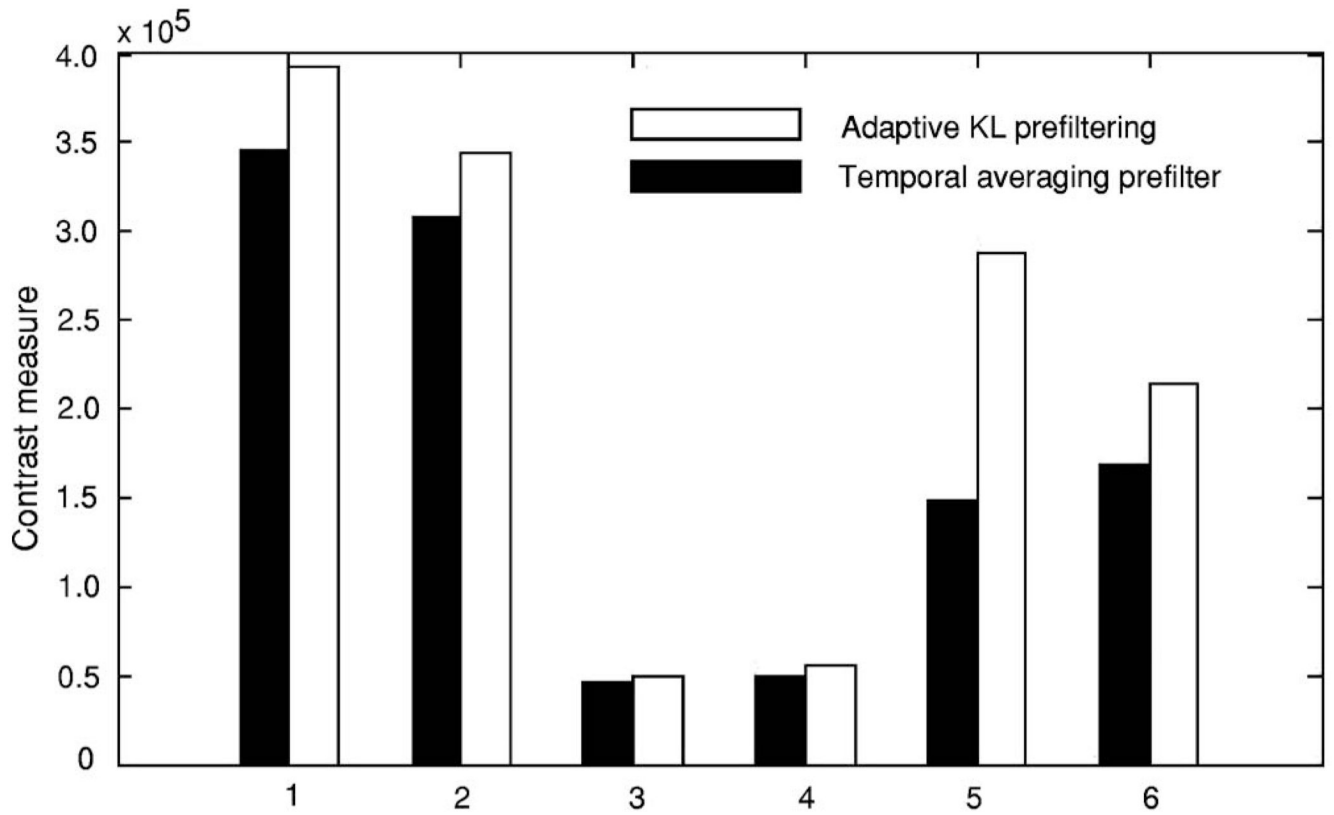
(e) Restored after temporal-average prefiltering



(f) Restored after adaptive KL prefiltering

Fig. 6.

Image of a random cotton fiber (a) and lamina cribrosa optical section at 60 mmHg IOP level (d) restored using inverse filter deconvolution after prefiltering the image random artifacts using temporal-averaging filter and adaptive KL filter.



1-5 : Random cotton fibers

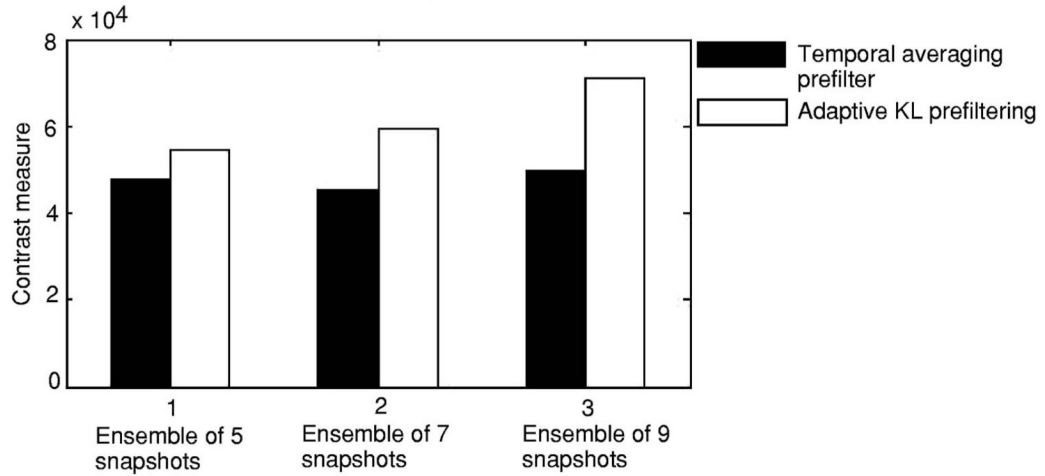
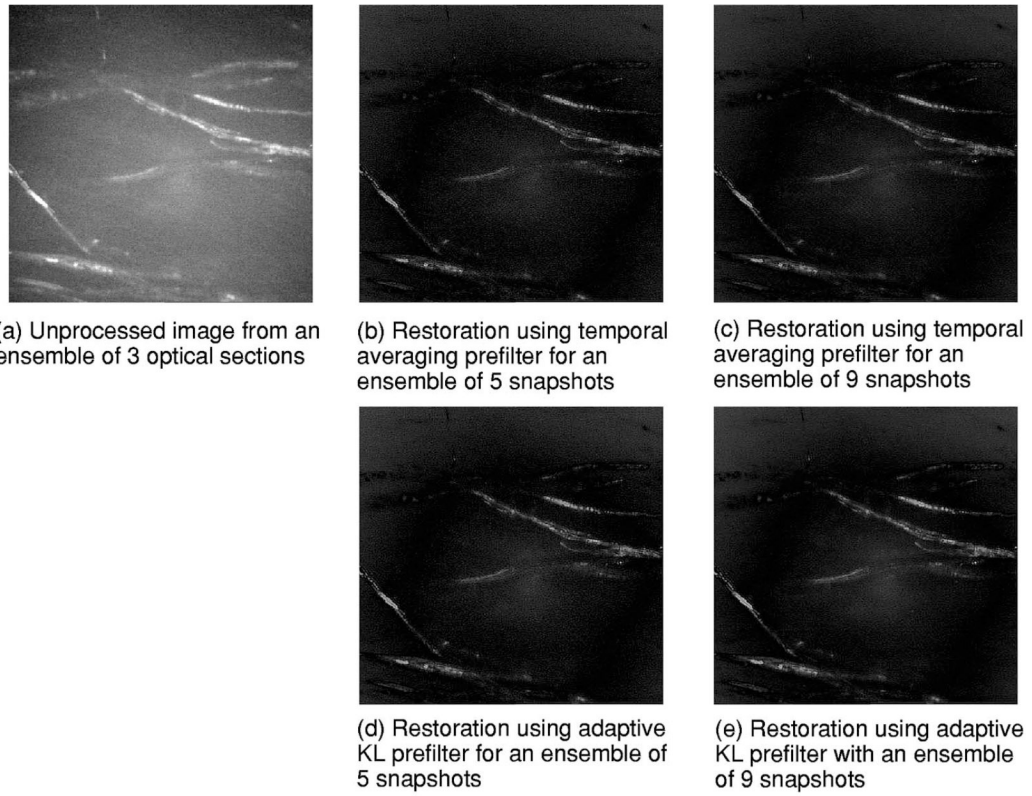
(**1** : Fig 4g & 4h; **2** : Fig 5b & 5c; **3** : Fig 5e & 5f; **4** : Fig 5h & 5i; **5** : Fig 6b & 6c)

6 : Lamina cribrosa at 12mmHg IOP level

(**6** : Fig 6e & 6f)

Fig. 7.

Contrast measure performance comparison of temporal-average and adaptive KL prefilters while restoring the optical section images using inverse restoration algorithm.



(f) Contrast measure plot comparing effect of ensemble size on the performance of temporal averaging prefilter and adaptive KL prefilter

Fig. 8. Effect of ensemble size in the performance of restoration with the temporal averaging prefilter and adaptive KL prefilter. Optical section ensembles of size 5, 7, and 9, acquired at the same z -axis position of a random cotton fiber, were used. There is an increase in the performance of adaptive KL prefilter with the increase in the number of optical sections used at the prefiltering stage.

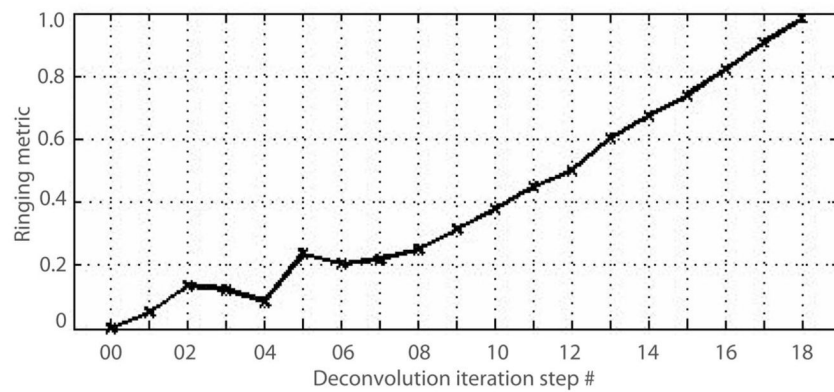
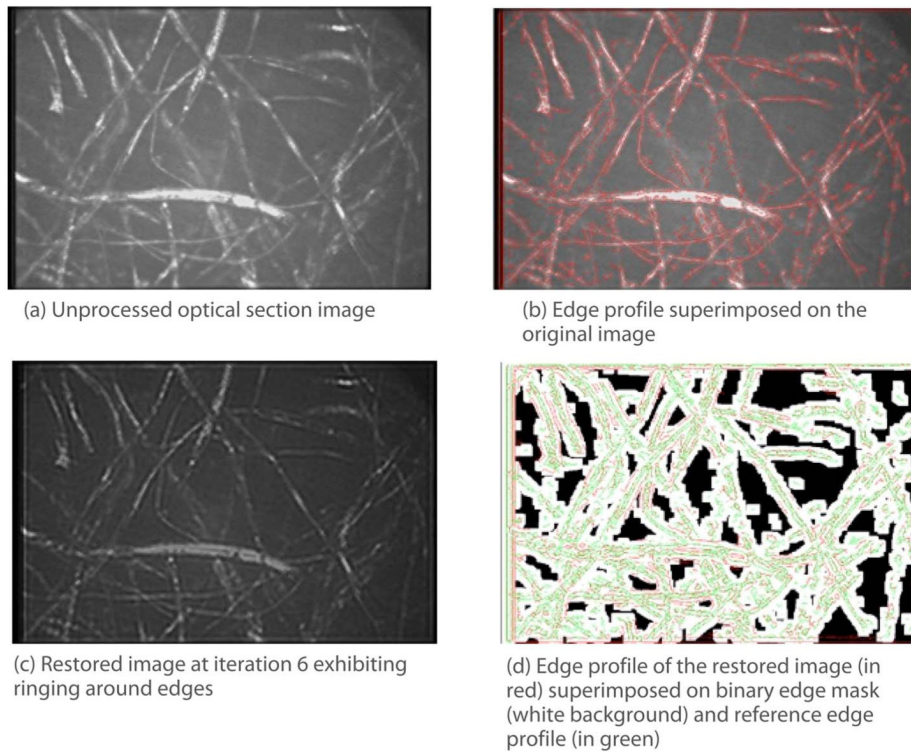


Fig. 9. Computing the ringing metric of an image restored using the LR iterative restoration algorithm. (color online only)